Kinetically Controlled Linker Binding in Rare Earth-DOBDC MOFs, and its Predicted Effects on Acid Gas Adsorption

Journal:	*ACS Applied Materials & Interfaces*
Manuscript ID	am-2021-17670g.R2
Manuscript Type:	Article
Date Submitted by the Author:	02-Nov-2021
Complete List of Authors:	Henkelis, Susan; Sandia National Laboratories, Nanoscale Sciences Department Vogel, Dayton; Sandia National Laboratories, Nanoscale Sciences Metz, Peter; Oak Ridge National Laboratory, Neutron Scattering Division Valdez, Nichole; Sandia National Laboratories Rodriguez, Mark; Sandia National Laboratories, Materials Characterization Rademacher, David; Sandia National Laboratories Purdy, Stephen; Oak Ridge National Laboratory, Neutron Scattering Division Percival, Stephen; Sandia National Laboratories, Electronic, Optical and Nanoscale Materials Rimsza, Jessica; Sandia National Laboratories, Geochemistry Page, Katharine; University of Tennessee Knoxville College of Engineering, Materials Science and Engineering Department Nenoff, Tina; Sandia National Laboratories, ; Sandia National Laboratories Technical Library,

Kinetically Controlled Linker Binding in Rare Earth-DOBDC MOFs, and its Predicted Effects on Acid Gas Adsorption

Susan E. Henkelis,[a] Dayton J. Vogel,[a] Peter C. Metz,[b] Nichole R. Valdez,[c] Mark A. Rodriguez,[c] David X. Rademacher,[a] Stephen Purdy,[b] Stephen J. Percival,[d] Jessica M. Rimsza,[e] Katharine Page,[b,f] Tina M. Nenoff*[g]

a. Nanoscale Sciences Department, Sandia National Laboratories, Albuquerque, NM 87185, USA.

b. Neutron Scattering Division, Oak Ridge National Laboratory, Oak Ridge, TN 37831, USA.

c. Materials Characterization and Performance Department, Sandia National Laboratories, Albuquerque, NM 87185, USA

d. Electronic, Optical and Nano Materials Department, Sandia National Laboratories, Albuquerque, NM 87185, USA

e. Geosciences Engineering Department, Sandia National Laboratories, Albuquerque, NM 87185, USA

f. Materials Science and Engineering Department, University of Tennessee, Knoxville, TN 37912, USA

g. Material, Physical, and Chemical Sciences Center, Sandia National Laboratories, Albuquerque, NM 87185, USA, New Mexico 87185, USA.

Key Words: Metal-organic framework, MOF, Kinetics, NO_x adsorption, Acid gas, Modelling

ABSTRACT: In the pursuit of highly stable and selective metal-organic frameworks for the adsorption of caustic acid gas species, an entire series of rare-earth metal organic frameworks (MOFs) have been explored. Each of the MOFs in this series (RE-DOBDC; RE = La, Ce, Pr, Nd, Sm, Eu, Gd, Tb, Dy, Ho, Er, Tm, Yb, Lu; DOBDC = 2,5-dihydroxyterepthalic acid) were synthesized in the tetragonal space group *I4/m*. Crystallized MOF samples, specifically Eu-DOBDC, were seen to have a combination of monodentate and bidentate binding when synthesized under typical reaction conditions, resulting in a contortion of the structure. However, extended crystallization times determined that this binding is kinetically controlled, and that the monodentate binding option was crystallographically eliminated by extended reaction times at higher temperatures. Furthermore, this series allows for the direct study of the effect of the metal center on the structure of the of the MOF; herein, the lanthanide metal ionic radii contraction across the periodic table results in a reduction of the MOF pore size and lattice parameters. Scanning electron microscopy – energy dispersive spectroscopy (SEM-EDX) was used to investigate the stages of crystal growth for these RE-DOBDC MOFs. All MOFs, except Er-DOBDC had a minimum of two stages of growth. These analogs were demonstrated by analysis of neutron diffraction (PND) to exhibit a cooperative rotational distortion of the SBU, resulting in two crystallographically distinct linker sublattices. Computational modelling efforts were used to show distinct differences on acid gas (NO_2, SO_2) binding energies for RE-DOBDC MOFs when comparing the monodentate/bidentate combined linker with the bidentate-only linker crystal structures.

Introduction

Metal-organic frameworks (MOFs) are 2- or more typically 3-dimensional porous solids made from connecting organic linkers and metal cations or clusters.[1–5] Due to their unique connectivity, some MOFs have coordinated unsaturated metal sites (CUSs) that allow for target molecules to bind. As such, MOFs have application space in sensing,[6–11] catalysis,[12–16] gas storage and release,[17–23] and gas separation. Materials design through the combination of modelling and experiments allows for MOFs with uniquely tuned attributes such as pore size and shape, and metal center to be created for a specific application.[24,25]

During MOF synthesis, the deprotonated linker and hydrolysed solvent reversibly crystallise with the MOF crystallite precursors to form the final 3-dimensional MOF.[26] Consequently, the concentration of these components can affect the structure of the MOF grown. Therefore, the kinetics of nucleation and crystallization during MOF synthesis can be investigated by varying conditions such as reagent ratios, temperature and reaction time length.[26–28] For example, solvothermal synthesis of MOFs at low temperature slows down the nucleation kinetics which leads to a more controlled crystal growth. Growing MOFs at high temperature, speeds up the reaction which allows the MOFs to be synthesized in larger quantities over a shorter space of time. However, there is a trade-off between synthesizing large amounts and the potential reduction in crystallinity of the MOF produced.[27]

MOF synthesis kinetics can be controlled experimentally through the use of a monocarboxylic acid modulator such as

benzoic acid. The modulator competitively binds to the metal center without changing the stoichiometry of the MOF reagents, which slows down the nucleation kinetics to direct to one desired product.[29,30] Typically, the immediate product formed is the kinetically favoured product, due to the faster rates of nucleation and crystallization. This may differ from most thermodynamically stable products. Moreover, the addition of increased quantities of modulator increases the MOF crystallite size whilst increasing the product's crystallinity.[30]

One of the many uses of MOFs is gas separation. There are two main approaches to this: molecular sieving and preferential binding of one target gas over another. Molecular sieving allows for gas adsorption by size exclusion. Preferential binding however, is the selective binding of one target gas from a mixture through judicious selection of metal center and/or linker. For example, the selective adsorption of SO_x from a complex humid SO_x stream using Mg-MOF-74 via binding to the Mg cation.[17]

Flue gases contain ppm levels of toxic acid gases, such as NO_x and SO_x and are an important mixture for gas separation and storage as they are detrimental to the environment.[7,31–40,68-71] Recently, a series of RE-DOBDC (RE = Y, Eu, Tb, Yb; DOBDC = 2,5-dihydroxyterephthalic acid) MOFs have been synthesized and shown to adsorb NO_x from chemically generated humid NO_x streams, whose concentrations approximate a conventional flue stream. These MOFs have also been extensively studied to understand changes in both their optical and magnetic properties as a function of NO_x gas binding.[24,25,41,42]

Both modelling and experimental approaches on a set of RE elements (Y, Yb, Eu, Tb) were used to confirm NO_x binding to the linker, rather than to the metal center.[25,43] This was further verified computationally by analysing the electronic density of states. Through the use of density functional theory (DFT), predictions have been made on target acid gas binding to the metal centers, with the gas binding energies in order of $NO_2 < H_2O < SO_2$.[18]

We have expanded the study to include the entire rare earth family of elements and herein present the synthesis and characterization of all the RE-DOBDC (RE = La, Ce, Pr, Nd, Sm, Gd, Dy, Ho, Er, Tm, Lu; plus Y, Eu, Tb, Yb) MOFs. Although not a lanthanide, Y can be classified as a rare earth due to its similarity to the lanthanide series and therefore has been included in the data.

This study allows for the investigation into the linker-metal binding to enable crystallization in the same space group across the periodic table. It also enables the study of the role of cationic metal radii on the resulting MOF pore size, and to predict its effect on acid gas binding in the RE-DOBDC MOF series.

In particular, this series of MOFs was studied to examine the role of reaction time and kinetics in the formation of monodentate/bidentate (MD/BD@DOBDC) versus bidentate-only (BD@DOBDC) framework binding. Of specific interest is the analysis of how kinetically controlled linker binding may affect the adsorption of NO_x and SO_x from a humid gas stream. This is further elucidated via DFT modelling efforts.

Materials and Methods

All commercial reagents were used without any further purification. Synthesis conditions for La-DOBDC is presented below; conditions for all analogues can be seen in the SI.

Materials Synthesis

Synthesis of La-DOBDC: Lanthanum chloride heptahydrate (0.069 g, 0.188 mmol) and 2,5-dihydroxyterephathlic acid (0.054 g, 0.275 mmol) were dissolved with sonication in *N,N'*-dimethylformamide (4 mL). 2-fluorobenzoic acid (0.576 g, 4.11 mmol) was dissolved in *N,N'*-dimethylformamide (4 mL) and added to the salt solution. Water (2 mL) and nitric acid (0.6 mL, 3.5 M) were added to the reaction mixture and heated at 125 °C for 60 hr in a sealed 20 mL scintillation vial. The crystals were collected by filtration, washed with *N,N'*-dimethylformamide (2 x 50 mL) and water (2 x 50 mL), then dried on the filter with acetone (50 mL).

Powder X-ray Diffraction

Laboratory powder X-ray diffraction data were collected on a Siemens D500 Krystalloflex diffractometer (Bruker AXS, Inc. Madison, WI) operating CuKα1 radiation at 30 mA and 40 kV at room temperature in reflectance mode with a curved graphite crystal monochromator.

Scanning Electron Microscopy-Energy Dispersive Spectroscopy

Scanning Electron Microscopy (SEM) analyses were captured on a FEI NovaNano SEM 230, at various accelerating voltages between 1 – 20 kV. Energy Dispersive Spectroscopy (EDX) analyses were collected on an EDAX Genesis Apex 2 with an Apollo SDD detector.

Single Crystal X-ray Diffraction

Crystals of RE-DOBDC were mounted on a MiTeGen loop with superglue. Single crystal X-ray diffraction data were collected at 275 K on a Bruker APEX-II CCD diffractometer system (λ = 0.71073 Å). The structure solution was obtained using SHELXT [44] and refined by full-matrix least-squares on F2 using SHELXL.[45] The structure was finalized in OLEX2.[46] All full occupancy non-hydrogen atoms were refined with anisotropic atomic thermal displacement parameters. Aromatic hydrogen atoms were placed at their calculated positions using SHELXL.

Neutron Powder Diffraction

High resolution neutron powder diffraction data were collected using the instrument POWGEN [47] of the Spallation Neutron Source (SNS) at Oak Ridge National Laboratory (ORNL). Approximately 0.5 g powder samples of Y, Yb, and Tb DOBDC were loaded into standard 6 mm vanadium cans and sealed using a copper gasket. For each sample, isothermal data was collected at 300 K. Data were collected using the incident spectra centered at the longer wavelengths of 2.665 and 1.500 Å with Q-coverage (Q = 2π

/ d) of 0.3-5.9 and 0.5-12.9 $Å^{-1}$, respectively. Routine data reduction was performed using MANTID.[48]

We note the large powder crystalline samples for NDP were the product of combined reaction products. The final sample contained a mixture of crystallization stages of the RE-DOBDC MOFs and therefore a different structure interpretation than for the single crystals examined. This is discussed in detail below.

Computational Modelling

For calculated gas adsorption geometries, ground state electronic structures were optimized using spin unrestricted DFT as implemented in the Vienna Ab initio Simulation Package (VASP)[49,50] code in a plane wave basis set,[51,52] with projector-augmented wave (PAW) potentials.[53,54] Large core potentials (LCPs), which represent the M(III) oxidation state and place the Ln 4f electrons in the potential core, with a 600 eV cutoff energy and converged to a force accuracy of 0.03 eV/Å were used with a gamma point for k-point sampling. A Gaussian smearing of 0.01 eV was used for smearing of the electron occupation. The generalized gradient approximation (GGA) exchange correlation functional of Perdew, Burke, and Ernzerhof designed for solids and surfaces (PBEsol) [55] was chosen for consistency with recent successes in RE-MOFs.[25,42,56] The DFT-D3 method of Grimme [57] with Becke–Jonson damping [58] was added as a dispersion correction.

Based on previous studies, the following computational procedure was used as a reproducible process for optimizing RE-DOBDC MOF structural geometries when interchanging RE elements in the framework.[42,56] Initial geometries for the current calculation set are taken from the newly presented structures for Ce, Sm, Eu, Tb, Er, and Yb -DOBDC.[24,42,56,59–61] The structural relaxation of RE-DOBDC MOFs is a previously utilized multi-step process: 1) optimization of atomic positions 2) optimization of cell volume and atomic positions and 3) re-optimization of only atomic positions. Final energies used to calculate binding energies of the 3D RE-DOBDC systems were calculated in reciprocal space for increased accuracy. Optimization of gas adsorption to the RE metal sites were completed by placing H_2O, SO_2, or NO_2 molecules within a physisorption distance of 2-3 Å from the metal center with an O atom oriented toward the metal center. This gas orientation is consistent with the previously identified lowest energy configurations of gas binding with the Eu metal in Eu-DOBDC MOFs.[25] The entire MOF+gas system was then relaxed using the same parameters listed above for the pure MOF system. The binding energies of the systems were calculated as $E_{binding} = E_{MOF+gas} - E_{MOF} - E_{gas}$.[61] Energy of the gas molecule (E_{gas}) was calculated by simulating a single gas molecule in a 20 Å × 20 Å x 20 Å box, consistent with previous methodologies.[62]

Results and Discussion

The synthesis and crystallization of a family of MOFs containing the same geometric building block from across a series is not trivial. Here, the lanthanide metal cluster in a series of RE-DOBDC (RE = Y to Lu) MOFs has been realized; the series of isostructural MOFs has been synthesized and fully characterized.

Synthesis and Stability of Rare Earth Metal MOFs

Ten new RE-DOBDC MOFs containing Ce, Pr, Nd, Sm, Gd, Dy, Ho, Er, Tm, and Lu individual metal centers have been synthesized as large single crystals (40-70 μm). A modified synthesis procedure derived from the original synthesis procedures of RE-DOBDC MOFs (Y, Eu, Tb, Yb) was utilized.[25] Specific metal salt : linker : modulator (S:L:M) ratios were needed to crystallize each analogue; for example the ratio used for the Eu and Tb analogues is 1 : 1.46 : 21.86. Variations in reaction time and temperature were needed (Table 1) to ensure purity of phase formation. For example, while Y-DOBDC was crystallized in 3 days, the Er-DOBDC 3 day preparation resulted in a mixed phase. Only after 10 days was Er-DOBDC crystallized as a pure single phase.

An exhaustive study was undertaken to determine the exact parameters for a successful synthesis. This started by using the same conditions from the literature [25] before modifying reaction time length, temperature and amount of reagents until the optimum was found. It is not currently known why each lanthanide salt needs a different reaction condition to produce a pure material, however one can surmise that both sterics and electronics come in to play. As the lanthanide series progresses from La to Lu, the size of the cation ionic radius gets smaller, inducing steric strain in the MOF framework.[29] Furthermore, as the lanthanides contract, their basicity (ease at which they lose an electron) decreases from La>Lu, meaning their general reactivity to form complexes also decreases. Therefore, it stands to reason that the later lanthanides (Ho onwards) need more of the protonated linker present in the MOF solution in order to force an electron transfer from the cation, and therefore speed up the kinetics of the reaction.[25]

Table 1. Reaction conditions for both new and existing RE-DOBDC MOFs. The ratios of S:L:M for the existing MOFs are also inputted below.

Rare Earth	Molar ratio S:L:M	Temp (°C)	Days In Oven
Y	1 : 1.32 : 19.84	115	3
La	1 : 1.46 : 21.86	125	3-6
Ce	1 : 2 : 21.86	125	3
Pr	1 : 1.46 : 21.86	125	6
Nd	1 : 1.46 : 21.86	125	6
Sm	1 : 1.46 : 21.86	125	3
Eu	1 : 1.46 : 21.86	115	3
Gd	1 : 2 : 21.86	125	3
Tb	1 : 1.46 : 21.86	115	3
Dy	1 : 1.46 : 21.86	125	6
Ho	1 : 1.58 : 7.98	125	3
Er	1 : 1.58 : 7.98	125	10
Tm	1 : 2 : 7.98	125	3
Yb	1 : 1.58 : 7.98	115	3
Lu	1 : 1.58 : 7.98	125	3

Each MOF analogue crystallized as large (ca. 0.5 mm^3) single crystals and was analysed by single crystal X-ray diffraction (SCXRD), powder X-ray diffraction (PXRD), and the stages of crystal growth determined by scanning electron microscopy-energy dispersive spectroscopy (SEM-EDX). Additionally, three compositions in the RE-DOBDC series (RE = Y, Tb, Yb) were studied using high-resolution neutron powder diffraction (HR-PND) to better analyse both the 8/9-fold coordination of the metals found in the secondary building unit (SBU) of the MOF, and any structural distortion caused by metal cation radii size changes. Note, all isotopes of Pm are radioactive and therefore has been excluded from this study.

Each MOF was initially examined by powder X-ray diffraction to ensure both phase purity, crystallinity, and diffraction data match (Figure 1).[25] It is especially important to utilize powder diffraction to ensure that the simulated powder pattern from the single crystal data matches that of the bulk material and not just one particular crystal of a different phase.

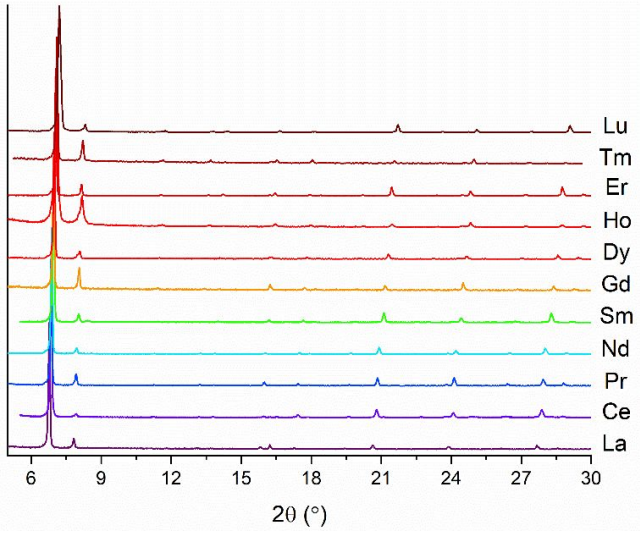

Figure 1. Experimental powder X-ray diffraction patterns for each new RE-DOBDC MOF. Patterns shown from bottom (La) to top (Lu) as the series progresses, highlighting the shift in pattern to increased 2θ. La – bright purple, Ce – dark blue, Pr – bright blue, Nd – teal – Sm – green Gd – yellow – Dy –orange – Ho – burnt orange – Er – red, Em – dark red, Lu – brown.

The RE-DOBDC MOFs series has been analysed for crystallographic similarities and differences. The rare earth metals' ionic radii are known to contract as the series progresses up in atomic number. Here, by choosing the rare earth (lanthanide) series as the metal center, the pore size of the MOF can be tuned with the change in the rare earth cation. This change in pore size can easily be seen by powder diffraction, with the whole pattern shifting to increased 2θ values (smaller cell volumes) as the series progresses from lanthanum to lutetium. This can be seen more clearly by focusing on the first sharp peak at 7 ° 2θ. This peak represents the [101] hkl (d_{101}) spacing, which corresponds to the faces of the quasi-octahedral pore. The d_{101} peak shift correlates in a linear fashion with the contraction of the ionic radii, as seen in Figure 2. This shift in peak and reduction in pore volume occurs due to a local distortion in the framework. This allows accommodation for the different sizes of lanthanide whilst maintaining the same structure.

Powder X-ray diffraction was also implemented to characterize the stability of each RE-DOBDC phase after exposure to a number of environments. The crystalline powder samples were allowed to sit undisturbed under ambient conditions in a borosilicate vial for up to 6 months and remained crystalline. They have also been characterized as bench stable in humidity (ca. 40% RH) and also in many polar aprotic and non-polar solvents. However, when the MOF is placed in liquid water, the framework begins to break down, as seen by a change in PXRD and luminescence. This has been seen in recent work regarding Mn-DOBDC, whereby the MOF dissolves, leaving the protonated DOBDC linker in solution, whilst the RE salt precipitates out.[25] This produces a bright yellow fluorescence from the linker.

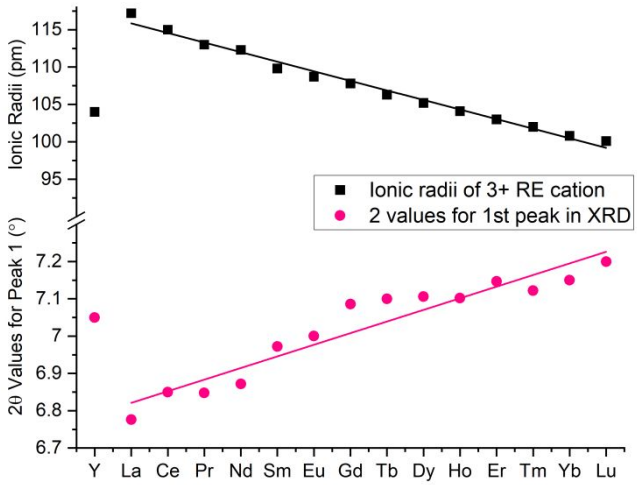

Figure 2. The linear correlation between lanthanide ionic radii contraction (top – black squares) and the corresponding d_{101} peak for each lanthanide (bottom – pink squares). Both data sets are fit with a linear fit.

Single Crystal X-ray Diffraction Reveals Unique Linker Binding

To further analyse the crystallography of the materials, select MOFs from regular positions across the series were investigated by single crystal X-ray diffraction: Ce, Sm, Eu, Tb, Er, Yb, with each MOF collected in the tetragonal space group *I4/m*. The crystallographic data including lattice parameters, data collection and refinement parameters are summarized in Table 2. Related cif files are found in the SI. All cifs can be found in the CCDC under the following codes: 2045642 (Ce), 2045523 (Sm), 2057754 (Eu), 2045856 (Tb), 2045649 (Er), 2045857 (Yb).

Although Tb- and Yb-DOBDC have been previously synthesized and powder X-ray data refinement reported in earlier papers,[25] the single crystal data had not been collected and thus is reported for the first time here. Eu-DOBDC has been previously collected; it has been recollected in this work to show quality data describing a unique binding phenomenon throughout the structure. This is described in detail below.

Novel Ce-DOBDC, Sm-DOBDC and Er-DOBDC have been synthesized for the first time and have been collected as large single crystals in space group *I4/m*. From the single crystal data, a clear contraction in both cell volume and unit cell parameters can been seen from Ce to Yb, with a contraction in cell volume from 5440.9(3) to 4781.4(4) Å^3 and contraction in the a=b lattice parameters from 15.6696(3) to 15.0084(5) Å.

Table 2. Crystallographic data collection and structure refinement results for RE-DOBDC (RE = Ce, Sm, Eu, Tb, Er, Yb)

MOF	Ce-DOBDC	Sm-DOBDC	Eu-DOBDC	Tb-DOBDC	Er-DOBDC	Yb-DOBDC
Formula	$C_{24}e_3O_{25}$	$C_{24}Sm_3O_{25}$	$C_{24}Eu_3O_{25}$	$C_{24}Tb_3O_{25}$	$C_{24}Er_{3250}$	$C_{24}Yb_3O_{25}$
fw (gmol^{-1})	4446.50	4569.26	4576.48	4672.10	4772.18	4841.54
Temperature (K)	275	275	275	275	275	275
Crystal System	Tetragonal	Tetragonal	Tetragonal	Tetragonal	Tetragonal	Tetragonal
Space Group	*I4/m*	*I4/m*	*I4/m*	*I4/m*	*I4/m*	*I4/m*
a (Å)	15.6696(3)	15.356(2)	15.3039(3)	15.2296(9)	15.0967(4)	15.0084(5)
b (Å)	15.6696(3)	15.356(2)	15.3039(3)	15.2296(9)	15.0967(4)	15.0084(5)
c (Å)	22.1594(8)	21.737(5)	21.6465(7)	21.4734(17)	21.3501(8)	21.2270(12)
α=β=γ (°)	90	90	90	90	90	90
V (Å^3)	5440.9(3)	5125.8(19)	5069.8(3)	4980.6(7)	4865.9(3)	4781.4(4)
Z	4	4	4	4	4	4
ρ_{calcd} (gcm^{-1})	1.357	1.480	1.499	1.558	1.629	1.681
F(000)	2084	2132	2132	2168	2204	2228
Crystal Size (mm^3)	0.6 x 0.6 x 0.6	0.5 x 0.4 x 0.4	0.5 x 0.4 x 0.4	0.5 x 0.5 x 0.5	0.5 x 0.5 x 0.5	0.2 x 0.2 x 0.1
Theta range (°)	5.647-72.072	2.651-25.960	3.121-26.060	3.138-29.129	3.165-25.967	1.919-27.877
Limiting Indices	$-19 \le h \ge 19$	$-18 \le h \ge 18$	$-18 \le h \ge 18$	$-20 \le h \ge 20$	$-18 \le h \ge 18$	$-19 \le h \ge 19$
	$-19 \le k \ge 18$	$-18 \le k \ge 18$	$-18 \le k \ge 18$	$-20 \le k \ge 20$	$-18 \le k \ge 18$	$-19 \le k \ge 19$
	$-27 \le l \ge 27$	$-26 \le l \ge 26$	$-26 \le l \ge 26$	$-29 \le l \ge 29$	$-26 \le l \ge 26$	$-27 \le l \ge 27$
GOF	1.311	1.184	1.212	1.181	1.122	1.153
R (all data)	R_1 = 0.0679	R_1 = 0.0703	R_1 = 0.0281	R_1 = 0.0843	R_1 = 0.0243	R_1 = 0.0341
	wR_2 = 0.1613	wR_2 = 0.1837	wR_2 = 0.0818	wR_2 = 0.2093	wR_2 = 0.0714	wR_2 = 0.0897

All RE-DOBDC MOFs synthesized and reported here are comprised of a secondary building unit (SBU) $RE_6O_4(OH)_4$ in which the triangular faces of the RE_6-octahedron are alternatively capped by μ_3-O and μ_3-OH groups. The inner $RE_6O_4(OH)_4$ core is bridged by 12 carboxylate groups originating from the 2,5-dihydroxyterephthalic acid (DOBDC) linker.

As the size of the rare earth cation decreases, so does the size of the cluster and therefore as a result, the size of the triangular pore window decreases as the lanthanide series progresses from left to right. Each carboxylic oxygen (1 and 2 in Figure 3) covalently binds to 2 distinct RE atoms (a and b in Figure 3) in the octahedral cluster, anchoring a 3-dimensional supramolecular tetragonal lattice with octahedral pores that are accessible through triangular windows (Figure 3).

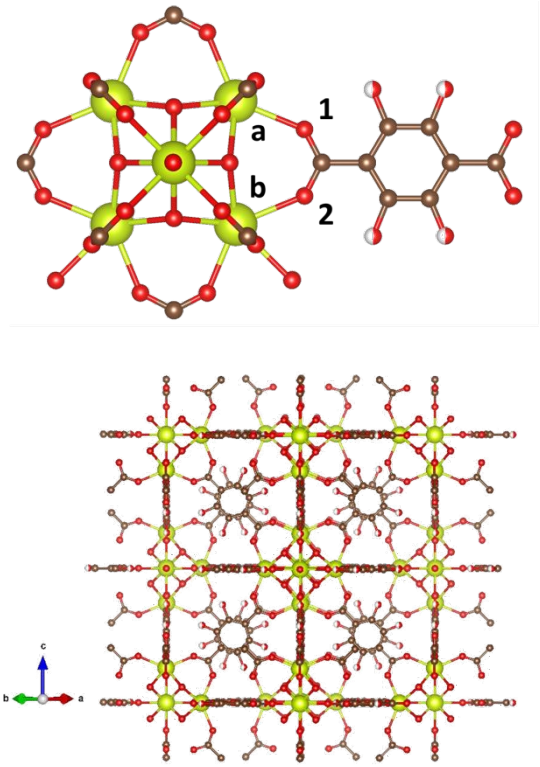

Figure 3. The bidentate binding of the DOBDC linker to the Ce octahedral cluster in Ce-DOBDC (top) and the 3-dimensional framework as viewed parallel to the *c* plane (bottom). C – brown, O – red, Ce – yellow. The hydrogen atoms are modelled as split occupancy. The phenolic groups on the linker have been modelled with split occupancy on each carbon (C2, C3, C5, C6). Individual metal cations have been labelled a and b, highlighting the binding to 2 individual carboxylic oxygen's (1 and 2).

Crystal Growth Steps

To elucidate the crystal growth steps of RE-DOBDC MOFs, we implemented scanning electron microscopy – energy dispersive spectroscopy (SEM-EDX). Crystal growth data were realized by studying the morphology of each MOF after a reaction time of 3-10 days (dependent on MOF) and isolated from the mother liquor by filtration.

Multiple stages of crystal growth could be seen from the initial MOF precursor to the large single crystal. Importantly, there was no observed change in the powder X-ray diffraction patterns throughout this process. The final crystalline phases of each MOF boasted the same prismatic morphology, with large crystals of ca. 50 nm (Figure S2).

All new RE-DOBDC MOFs synthesized here, except Er-DOBDC, have a minimum of 2 stages of crystal growth visible by SEM after 3-6 days reaction time at 125 °C. As the SEM is collected after the final MOF product has crystallized, it is anticipated that we have monitored all stages of growth. The preliminary stage (stage 1) is seen as nodular balls, and the final stage as individual, large single crystals. Nd-DOBDC, however, shows the most stages of crystal growth, with 4 visible by SEM. In stage 1, the morphology can be seen as nodular balls that look "cotton-ball" like. The balls clump together and due to the "fluffy" nature, we anticipate that this is the preliminary stage of crystallization, where after nucleation, the linker is beginning to bind to individual metal cations. This is corroborated with the increased amount of metal in the EDX quantification (Table 3). In stage 2, the nodular balls are starting to solidify as the MOF begins to grow into a 3-dimensional framework. As the framework begins to grow the metal cation content decreases from 91.93 to 87.56 wt% as more linkers are covalently binding to the metal. At stage 3, the MOF has fully formed as small, aggregated single crystals, with clearly defined facets. Finally, as the small crystals continue to grow in size, they reach stage 4 and are no longer aggregated with individual crystals reaching sizes of ca. 50 nm (Figure 4).

Each stage was further analysed by EDX to investigate the elemental composition as a function of crystal growth (Table 3). Er-DOBDC was the only MOF afforded that contained a singular phase of crystal growth as single crystals. It is anticipated that the increased reaction time from 3-6 days to 10 days, allowed for each preliminary phase, nodular or aggregate to fully react.

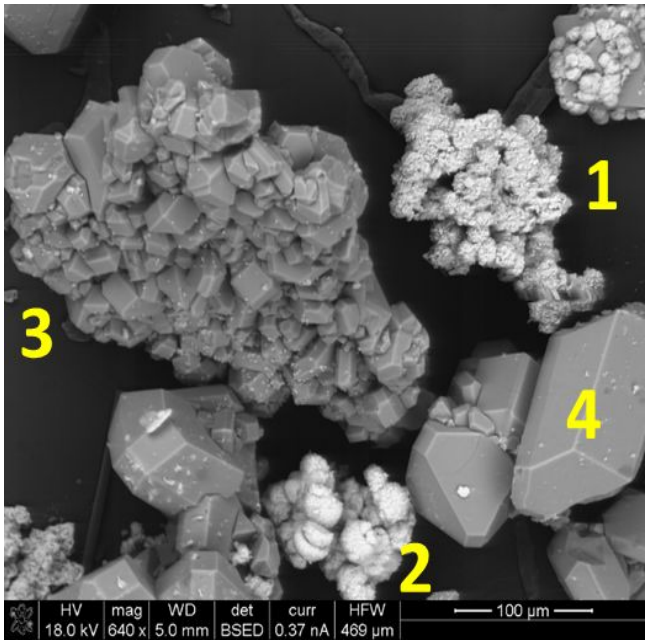

Figure 4. SEM image for Nd-DOBDC at 100 µm. 4 stages of crystal growth can be seen in Nd-DOBDC, with each highlighted by a yellow number. 1 = nodular, 2 = nodular balls, 3 = aggregates, 4 = single crystal.

Table 3. Elemental quantification for each stage of crystal growth for both Nd-DOBDC and Er-DOBDC. "-" = not found/ not present.

	Nd-DOBDC			Er-DOBDC
Element	Weight %	Phase	Element	Weight %
Nd	91.93	Nodular	Er	-
O	8.07		O	-
Nd	87.56	Nodular Balls	Er	-
O	12.42		O	-
Nd	78.10	Aggregates	Er	-
O	21.90		O	-
Nd	77.57	Single Crystal	Er	73.57
O	22.43		O	26.43

The progression through the phase development, can also be monitored by elemental analysis. It is clear that the quantity of Nd relative to O increases from 8.07 wt% to 22.43 wt% as the stage of crystal growth increases. It is anticipated that the relative amounts of Nd are lower in the preliminary phase (stage 1 – nodular) as at this stage, the Nd cation is beginning to bind to individual linkers. As the crystallography progresses, more of the Nd cation binds to the linkers until a threshold is reached, ultimately forming the full 3-dimensional framework. The quantities of each element for both the aggregates and the single crystal however, are roughly the same. This is anticipated, as although the aggregates are smaller and joined together, the MOF itself has fully formed. With longer reaction times these aggregated crystals will continue to grow and become larger crystals that are neither twinned nor aggregated, as seen in Er-DOBDC.

Kinetically Controlled Denticity

Earlier RE-DOBDC MOFs synthesized and characterized were shown to have a disordered linker binding, whereby not all of the carboxylates on the ligand were binding to the metal centers.[25] The tailored syntheses reported here show all members of the RE-DOBDC series have pure bidentate linker binding to the metal centers, herein called BD@DOBDC. This is confirmed herein by single crystal X-ray and powder diffraction data analysis.

As the disorder is more prominent in Eu-DOBDC, and the single crystal data for both the non-disordered and disordered has been collected, Eu is used as a representative disordered structure herein. In this work, Eu-DOBDC is shown to have a binding phenomenon between the linker and the metal center, whereby 50% of the linkers bind in a monodentate fashion and 50% bind in a bidentate fashion (Figure 5), in an ABAB manner; herein called MD/BD@DOBDC.

When bidentate-only bound, each carboxylate oxygen binds to individual Eu cations. This allows the linker to remain planar without introducing flexion to the structure. This ABAB pattern of binding is clear to see in both the single crystal and the powder X-ray diffraction. The occupancy of the C atoms was confirmed to ensure they were 100% bound to the linker. When the linker was previously found to be bound in a mixed monodentate/bidentate manner, both carboxylate oxygens from 1 carboxylate group are bound in a monodentate fashion to the same Eu cation in the cluster, which causes the linkers to bend and flex within the 3-dimensional structure (Figure 6).

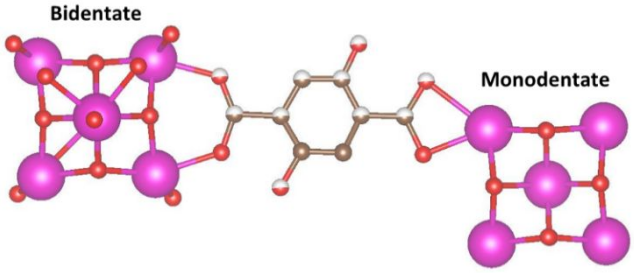

Figure 5. The monodentate binding of both carboxylate oxygens to 1 Eu cation in MD/BD@DOBDC (right) vs the bidentate binding (BD@DOBDC) of each carboxylate oxygen to individual Eu cation (left) in an ABAB manner.

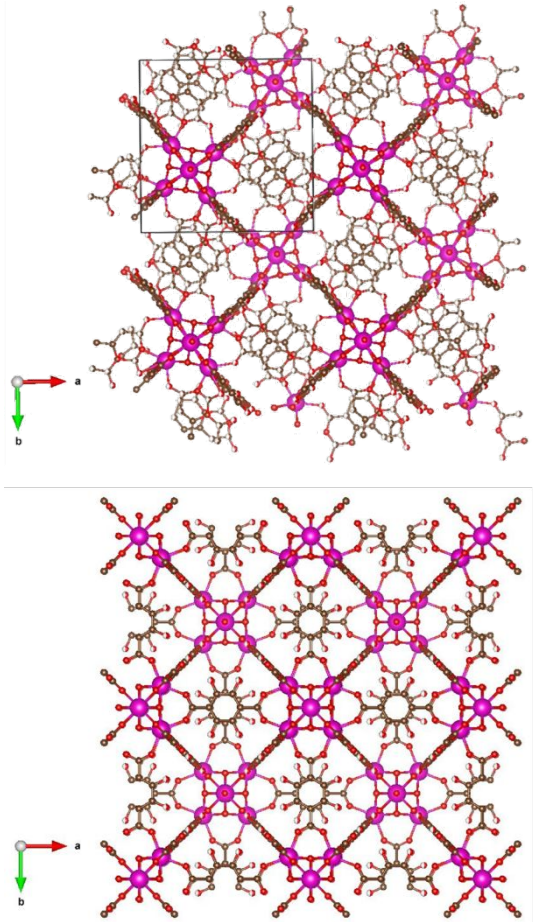

Figure 6. Comparison of BD@DOBDC Eu-DOBDC (BOTTOM) against the 3-dimensional supramolecular structure of MD/BD@DOBDC Eu-DOBDC (TOP), with each linker displaying a concave/convex arrangement, due to monodentate binding to the metal center. The unit cell has been highlighted by the black square. As viewed down the c axis. C – brown, O – red, Eu – pink.

To monitor the MD/BD@DOBDC transitioning to 100% bidentate binding (BD@DOBDC), powder X-ray diffraction of the bulk materials was conducted and compared against

both the calculated data from the BD@DOBDC Eu-DOBDC and the MD/BD@DOBDC Eu-DOBDC. It is apparent that although the majority of the powder pattern is identical, there is a small but consistent and unique change at 8.07 ° 2θ, corresponding to the (101) Bragg reflection. This sharp peak at 8.07 ° 2θ in the BD@DOBDC calculated pattern, splits in to two distinct peaks at 7.95 ° and 8.23 ° 2θ with the presence of monodentate binding seen in MD/BD@DOBDC (Figure 7).

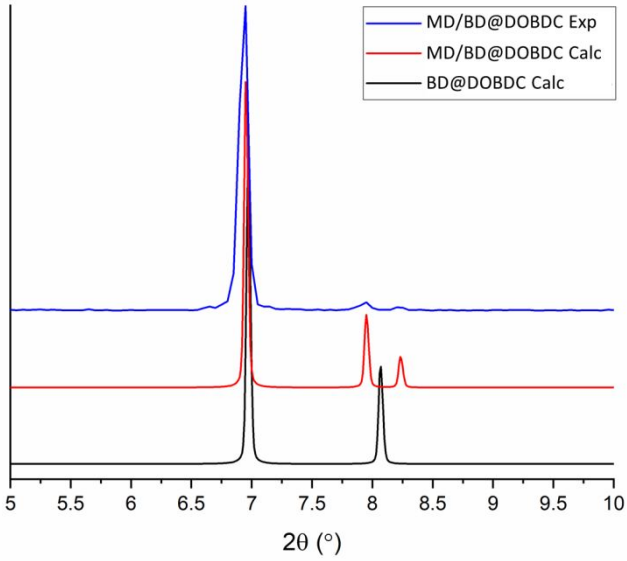

Figure 7. Powder X-ray diffraction patterns for the calculated BD@DOBDC (black), calculated MD/BD@DOBDC (red) and experimental MD/BD@DOBDC Eu-DOBDC (blue).

Investigations into the crystallization kinetics of MOF growth were undertaken to analyse the conversion from MD/BD@DOBDC to BD@DOBDC with increasing reaction time length and increasing temperature. Samples of Eu-DOBDC were synthesized under traditional solvothermal conditions with increasing time length from 3 to 10 days at 115 °C and 4 days at 125 °C. From the data collected, all batches synthesized at 115 °C for 3 days contained both types of linker binding to form MD/BD@DOBDC. Increasing the reaction time to 4 days at 115 °C removed the presence of the split peaks caused by the monodentate binding. This resulted in a singular broad peak to form BD@DOBDC. Furthermore, increasing the reaction time further to 5 days caused the monodentate binding to return, and after 10 days at 115 °C, the MOF framework was shown to begin to collapse crystallographically. The split peak caused by the monodentate binding had grown in intensity, suggesting more of the structure is now monodentate bound, causing a structural instability. Finally, upon increasing both the temperature to 125 °C and the reaction time to 4 days proved the best for eliminating the monodentate binding. By PXRD, the appearance of the split peak has completely merged back into 1 peak to form BD@DOBDC (Figure 8). Thus, we observe evidence of kinetically-controlled linker denticity in the RE-DOBDC series, especially for Eu-DOBDC.

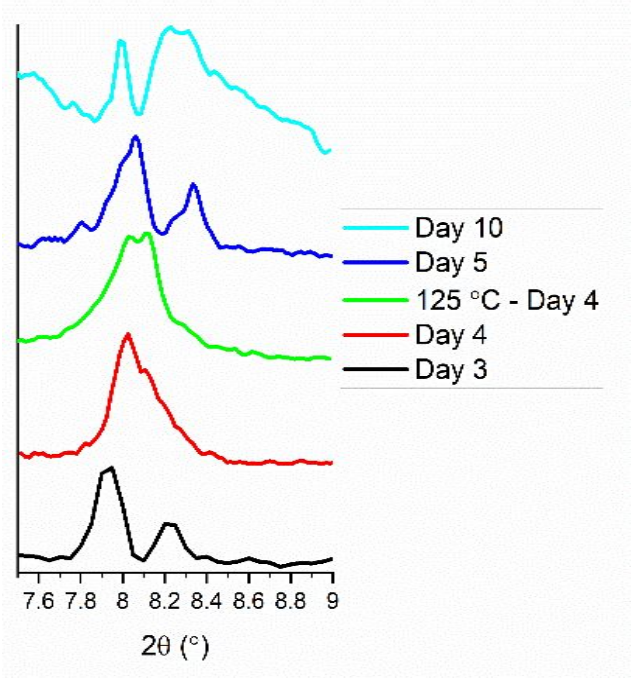

Figure 8. Experimental powder X-ray diffraction patterns for different batches of Eu-DOBDC synthesized at 115 °C for 3 days (black), 115 °C for 4 days (red), 115 °C for 5 days (blue), 115 °C for 10 days (aqua) and 125 °C for 4 days (green).

Neutron Diffraction is Consistent with Linker Denticity Observed

Powder neutron diffraction (PND) was undertaken and given the discrepancy between the previously reported 62 space group setting for Eu-DOBDC (P4/mnc) and that identified in this work (SI Table 2, I4/m BD@DOBDC; P1 MD/BD@DOBDC), the indexing evident in the neutron powder diffraction data was examined in depth. This was used to confirm that the neutron powder diffraction data are consistent with a rotational disordering mechanism that results in two distinct linker sites.

Rotation of the SBU is concomitant with the 4 linkers lying in the mirror plane normal to the rotation vector (here notated "equatorial"), and the magnitude of rotation scales linearly with the RE cation size. This linker rotation appeared favourable in contrast with a translational displacement disorder, suggesting the mean equatorial linker position is nearer the nominal (0, ½, 0) coordinate. In addition to this rotation, large anisotropic displacement in the equatorial linker and an apparent linker vacancy population are suggestive of a highly disordered site not fully described by this periodic model. In contrast, the 8 non-equatorial linker sites refine to the nominal (¼, ¼, ¼) centroid position bridging SBUs at the primitive and body centered positions with reasonable ADP values (Figure 9).

This differs somewhat from the structure obtained by single crystal X-ray diffraction. It seems likely the discrepancy is explained by the kinetics of crystallization,

with the large sample synthesized for neutron powder diffraction corresponding with an intermediate growth stage, discussed earlier.

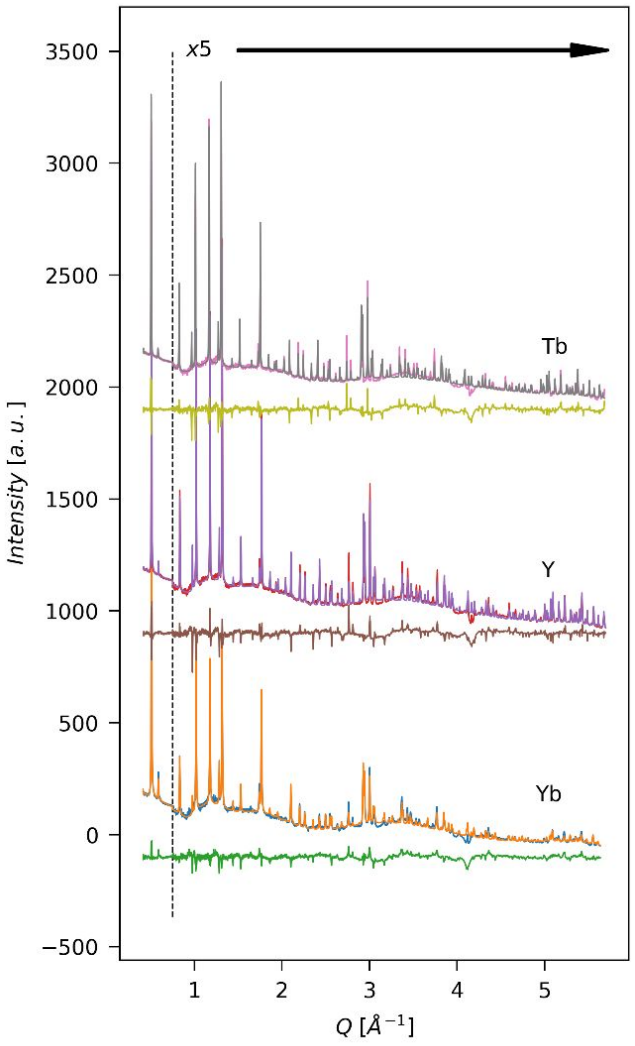

Figure 9. Rietveld refinements for the Tb-, Y-, and Yb-DOBDC neutron powder diffraction data (2.665 Å frame, POWGEN).

Computational Modelling Suggest that Linker Denticity Increases Acid Gas Adsorption

Understanding how the BD@DOBDC MOFs relate to the MD/BD@DOBDC MOFs is critical for future adsorption studies. As such, computational materials design studies have been incorporated throughout the RE-DOBDC MOF studies. Importantly, the newly discovered phases of RE-DOBDC MOFs resulted in fully bidentate DOBDC (BD@DOBDC) coordination, provide a new gas adsorption environment compared to the previously identified MD/BD@DOBDC MOF-linker coordination. Previously calculated acid gas binding energies across the Ln series identified unique secondary interactions formed between a gas adsorbed at an unsaturated metal site and a neighboring DOBDC hydroxyl group. The additional hydrogen bond formed between the adsorbed gas resulted in a strengthened adsorption energy.[25]

In the BD@DOBDC MOF structures, the binding energy follows the trend of NO_2 > SO_2 > H_2O, with calculated binding energies of -20 to -40 kJ/mol for NO_2, -20 to -65 kJ/mol for SO_2, and -90 to -100 kJ/mol for H_2O. The calculated gas adsorption energies for both MD/BD and BD@DOBDC phases of H_2O, NO_2, and SO_2 in Ce, Sm, Eu, Tb, Er, and Yb are presented in Figure 10. When compared with the binding energies in the MD/BD@DOBDC structures, there is an overall increase in the binding energies to less negative values in the BD@DOBDC MOFs. H_2O binding in the BD@DOBDC structure has a weaker binding energy of 4.7 kJ/mol on average across the calculated structures. The overall increase in binding energies is even more pronounced for NO_2 and SO_2 binding, with weakened binding energies by 50.5 and 51.3 kJ/mol respectively. Overall, the change in energies calculated for NO_2 and SO_2 are weakened by a factor of 10 compared to H_2O, indicating a change in either adsorption geometries or chemistry for NO_2 and SO_2.

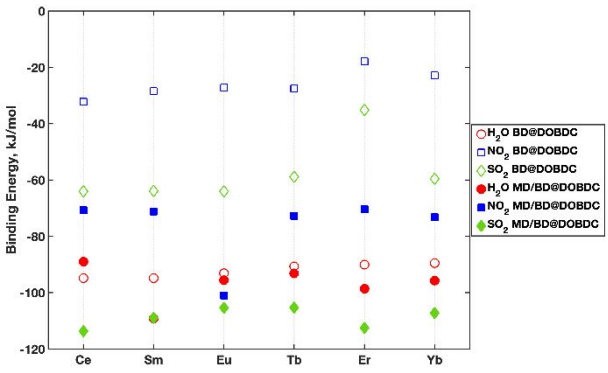

Figure 10. NO_2 (blue squares), H_2O (red circles), and SO_2 (green diamonds) calculated adsorption energies in RE-DOBDC MOFs with BD@DOBDC ligand binding (empty markers) and MD/BD@DOBDC ligand binding (filled markers).

Analysis of the gas adsorption geometries indicates the drastic drop in binding energy for NO_2 and SO_2, ~50 kJ/mol, results from a new binding interaction between the gas and BD@DOBDC. Specifically, the loss of the previously identified secondary hydrogen bond interaction, when adsorbed to the RE metal center, does not form in the new MOF phase. As H_2O adsorbs at the RE metal site via the O atom, the terminal H atoms cannot form secondary interactions with neighboring DOBDC linkers as seen in previous or current studies; this is due to its intrinsic size and binding geometry.[25] [67] NO_2 and SO_2 adsorb at the RE metal site via an O atom. However, the bend geometries of the molecules allow the opposite terminal O to interact with neighboring framework linkers. This is also in agreement conceptually with the size of H_2O versus NO_2 (and SO_2), as indicated by kinetic diameters of H_2O = 2.65 Å, NO_2 = 3.40 Å and SO_2 = 3.60 Å.[2564]

The calculated binding energies across the Ln series, H_2O, NO_2, and SO_2 also exhibit a trend of decreasing binding energy with larger Z values. As Z increases across the Ln series, the lattice parameter also decreases as expected for the known Ln contraction.[65,66] The change in adsorption behavior for H_2O, NO_2, and SO_2 is further exhibited by comparing the gas binding distances (SI Tables 3 and 4). Across the Ln series H_2O binds at shorter distances, following the Ln contraction trend to remain intact. However, for NO_2 and SO_2 the adsorption distance increases as the lattice parameter decreases due to steric hinderance for the gas to access the smaller metal site. The two opposite trends between H_2O vs NO_2 and SO_2 further indicates H_2O has easier access to the RE metal site compared to the larger NO_2 and SO_2 molecules.[25]

Conclusion

In the pursuit of highly stable and selective metal-organic frameworks for the adsorption of caustic acid gas species, an entire series of RE-DOBDC (RE = La, Ce, Pr, Nd, Sm, Gd, Dy, Ho, Er, Tm, Lu) have been explored. They were successfully synthesized under solvothermal conditions with metal:linker reagent ratios dependent on their position within the lanthanide series. Each MOF crystallized in the tetragonal space group *I4/m*. Each RE metal cation is coordinated to two DOBDC linkers through a single carboxylate oxygen, with the full six cation cluster coordinating to twelve DOBDC linkers and six coordinated solvent molecules. These solvent molecules due not act as a scaffold, and therefore upon activation, the structure remains intact. Through both single crystal and powder X-ray diffraction, a clear contraction in pore size can be seen as the rare earth series progresses from left to right. From the PXRD data, there is a clear shift in the d_{101} peak to increased 2θ, which trends in a linear fashion in comparison to the rare earth 3^+ cation ionic radii. To understand the stages of crystal growth, each MOF was investigated by SEM-EDX, with clear stages of growth seen.

Eu-DOBDC displays an interesting linker binding that is under kinetic control. Under the standard synthesis conditions for Eu-DOBDC, the MOF undergoes both monodentate and bidentate binding between the Eu^{3+} and the carboxylate oxygens on the linker, thus causing a distortion in the MOF structure. This phenomenon is visualized through both single crystal and powder X-ray diffraction. Allowing the MOF to react for an extended period of time of 4 days and at higher temperature removes this monodentate binding, and allows the MOF to form as pseudo-cubic with bidentate binding only.

It is well known that the presence of guest species complicates absolute structure refinement of the framework in highly porous structures.[67] While this refinement does not necessarily resolve the structural motif of the RE-DOBDC framework in the highly tuned single crystals produced later on, it does provide an indication of the degree of disorder characteristic of the intermediate phase formed in this synthesis. This emphasizes the care that must be taken in mechanistic investigations of highly porous MOFs, where an apparently crystalline powder diffraction pattern may belie the degree of perfection.

Through computational modelling, it becomes apparent that the selectivity and stability of the RE-DOBDC MOFs for acid gas adsorption is determined by the extent of the ligand bonding. Herein, the study shows that the BD@DOBDC MOFs have projected lower binding energies and increased steric hinderance that inhibits NO_2 and SO_2 metal binding as compared to MD/BD@DOBDC MOFs. This helps guide ongoing and future laboratory experiments.

ASSOCIATED CONTENT

This material is available free of charge via the Internet at http://pubs.acs.org.
Synthetic procedure and characterization for all MOFs. SEM-EDX analysis for all MOFs. TGA data for Y-, Nd-, Eu-, Tb- and Yb-DOBDC. Crystallographic details for MD/BD@DOBDC Eu-DOBDC. Calculated gas binding energies and gas adsorption distances for each acid gas. Neutron diffraction information and refinement.

AUTHOR INFORMATION

Corresponding Author

* Tina M. Nenoff. tmnenof@sandia.gov

Author Contributions

All authors have given approval to the final version of the manuscript.

Funding Sources

This work was supported as part of the Center for Understanding and Control of Acid Gas-Induced Evolution of Materials (UNCAGE-ME), an Energy Frontier Research Center, funded by the U.S. Department of Energy (DOE), Office of Science, Office of Basic Energy Sciences under Award DE-SC0012577.

ACKNOWLEDGMENT

Sandia National Laboratories is a multimission laboratory managed and operated by National Technology and Engineering Solutions, LLC., a wholly owned subsidiary of Honeywell International Inc., for the U.S. Department of Energy's National Nuclear Security Administration under contract DE-NA-0003525. This paper describes objective technical results and analysis. Any subjective views or opinions that might be expressed in the paper do not necessarily represent the views of the U.S. Department of Energy of the United States Government.
This manuscript has been co-authored by UT-Battelle, LLC, under contract DE-AC05-00OR22725 with the US Department of Energy (DOE). The US government retains and the publisher, by accepting the article for publication, acknowledges that the US government retains a nonexclusive, paid-up, irrevocable, worldwide license to publish or reproduce the published form of this manuscript, or allow others to do so, for US government purposes. DOE will provide public access to these results of federally sponsored research in accordance with the DOE

Public Access Plan (http://energy.gov/downloads/doe-public-access-plan).

REFERENCES

(1) Peikert, K.; McCormick, L. J.; Cattaneo, D.; Duncan, M. J.; Hoffmann, F.; Khan, A. H.; Bertmer, M.; Morris, R. E.; Fröba, M. Tuning the Nitric Oxide Release Behavior of Amino Functionalized HKUST-1. *Microporous Mesoporous Mater.* **2015**, *216*, 118–126. https://doi.org/10.1016/j.micromeso.2015.06.020.

(2) Miller, S. R.; Alvarez, E.; Fradcourt, L.; Devic, T.; Wuttke, S.; Wheatley, P. S.; Steunou, N.; Bonhomme, C.; Gervais, C.; Laurencin, D.; Morris, R. E.; Vimont, A.; Daturi, M.; Horcajada, P.; Serre, C. A Rare Example of a Porous Ca-MOF for the Controlled Release of Biologically Active NO. *Chem. Commun. (Camb).* **2013**, *49* (71), 7773–7775. https://doi.org/10.1039/c3cc41987h.

(3) Grant Glover, T.; Peterson, G. W.; Schindler, B. J.; Britt, D.; Yaghi, O. MOF-74 Building Unit Has a Direct Impact on Toxic Gas Adsorption. *Chem. Eng. Sci.* **2011**, *66* (2), 163–170. https://doi.org/10.1016/j.ces.2010.10.002.

(4) Furchgott, R. F.; Ignarro, L. J.; Murad, F. The Nobel Prize in Physiology or Medicine 1998 http://www.nobelprize.org/nobel_prizes/medicine/laureates/1998/index.html/nhttp:/www.nobel.se/medicine/laureates/1998/illpres/ (accessed Oct 14, 2015).

(5) Collins, D. J.; Zhou, H.-C. Hydrogen Storage in Metal–Organic Frameworks. *J. Mater. Chem.* **2007**, *17* (30), 3154. https://doi.org/10.1039/b702858j.

(6) Henkelis, S. E.; Percival, S. J.; Small, L. J.; Rademacher, D. X.; Nenoff, T. M. Continuous Mof Membrane-Based Sensors via Functionalization of Interdigitated Electrodes. *Membranes (Basel).* **2021**, *11* (3), 1–15. https://doi.org/10.3390/membranes11030176.

(7) Small, L. J.; Henkelis, S. E.; Rademacher, D. X.; Schindelholz, M. E.; Krumhansl, J. L.; Vogel, D. J.; Nenoff, T. M. Near-Zero Power MOF-Based Sensors for NO2 Detection. *Adv. Funct. Mater.* **2020**, *30* (50), 2006598. https://doi.org/10.1002/adfm.202006598.

(8) DMello, M. E.; Sundaram, N. G.; Singh, A.; Singh, A. K.; Kalidindi, S. B. An Amine Functionalized Zirconium Metal-Organic Framework as an Effective Chemiresistive Sensor for Acidic Gases. *Chem. Commun.* **2019**, *55* (3). https://doi.org/10.1039/C8CC06875E.

(9) Yip, Y. W.; Law, G. L.; Wong, W. T. A Highly Selective On-off-on Responsive Lanthanide(III) Based Probe for Recognition of Copper and Hydrogen Sulfide. *Dalt. Trans.* **2016**, *45* (3), 928–935. https://doi.org/10.1039/c5dt03627e.

(10) Strauss, I.; Mundstock, A.; Treger, M.; Lange, K.; Hwang, S.; Chmelik, C.; Rusch, P.; Bigall, N. C.; Pichler, T.; Shiozawa, H.; Caro, J. Metal-Organic Framework Co-MOF-74-Based Host-Guest Composites for Resistive Gas Sensing. *ACS Appl. Mater. Interfaces* **2019**, *11* (15), 14175–14181. https://doi.org/10.1021/acsami.8b22002.

(11) Ferrando-Soria, J.; Serra-Crespo, P.; De Lange, M.; Gascon, J.; Kapteijn, F.; Julve, M.; Cano, J.; Lloret, F.; Pasán, J.; Ruiz-Pérez, C.; Journaux, Y.; Pardo, E. Selective Gas and Vapor Sorption and Magnetic Sensing by an Isoreticular Mixed-Metal-Organic Framework. *J. Am. Chem. Soc.* **2012**, *134* (37), 15301–15304. https://doi.org/10.1021/ja3045822.

(12) Pascanu, V.; González Miera, G.; Inge, A. K.; Martín-Matute, B. Metal-Organic Frameworks as Catalysts for Organic Synthesis: A Critical Perspective. *Journal of the American Chemical Society*. American Chemical Society April 11, 2019, pp 7223–7234. https://doi.org/10.1021/jacs.9b00733.

(13) Meyer, K.; Ranocchiari, M.; Van Bokhoven, J. A. Metal Organic Frameworks for Photo-Catalytic Water Splitting. *Energy and Environmental Science*. Royal Society of Chemistry July 1, 2015, pp 1923–1937. https://doi.org/10.1039/c5ee00161g.

(14) Comito, R. J.; Fritzsching, K. J.; Sundell, B. J.; Schmidt-Rohr, K.; DincĂ, M. Single-Site Heterogeneous Catalysts for Olefin Polymerization Enabled by Cation Exchange in a Metal-Organic Framework. *J. Am. Chem. Soc.* **2016**, *138* (32), 10232–10237. https://doi.org/10.1021/jacs.6b05200.

(15) Shen, J. Q.; Liao, P. Q.; Zhou, D. D.; He, C. T.; Wu, J. X.; Zhang, W. X.; Zhang, J. P.; Chen, X. M. Modular and Stepwise Synthesis of a Hybrid Metal-Organic Framework for Efficient Electrocatalytic Oxygen Evolution. *J. Am. Chem. Soc.* **2017**, *139* (5), 1778–1781. https://doi.org/10.1021/jacs.6b12353.

(16) Li, Z.; Schweitzer, N. M.; League, A. B.; Bernales, V.; Peters, A. W.; Getsoian, A. B.; Wang, T. C.; Miller, J. T.; Vjunov, A.; Fulton, J. L.; Lercher, J. A.; Cramer, C. J.; Gagliardi, L.; Hupp, J. T.; Farha, O. K. Sintering-Resistant Single-Site Nickel Catalyst Supported by Metal-Organic Framework. *J. Am. Chem. Soc.* **2016**, *138* (6), 1977–1982. https://doi.org/10.1021/jacs.5b12515.

(17) Henkelis, S. E.; Judge, P. T.; Hayes, S. E.; Nenoff, T. M. Preferential SOx Adsorption in Mg-MOF-74 from a Humid Acid Gas Stream. *ACS Appl. Mater. Interfaces* **2021**, *13* (6), 7278–7284. https://doi.org/10.1021/acsami.0c21298.

(18) Vogel, D.; Lee, Z.; Hanson, C.; Henkelis, S.; Smith, C.; Nenoff, T.; Dixon, D.; Rimsza, J. Predictive Acid Gas Adsorption in Rare Earth DOBDC Metal–Organic Frameworks via Complementary Cluster and Periodic Structure Models. *J. Phys. Chem. C* **2020,** *124* (49), 26801–26813. https://doi.org/10.1021/acs.jpcc.0c08282.

(19) Sava, D. F.; Chapman, K. W.; Rodriguez, M. A.; Greathouse, J. A.; Crozier, P. S.; Zhao, H.; Chupas, P. J.; Nenoff, T. M. Competitive I2 Sorption by Cu-BTC from Humid Gas Streams. *Chem. Mater.* **2013**, *25* (13), 2591–2596. https://doi.org/10.1021/cm401762g.

(20) Petit, C.; Mendoza, B.; Bandosz, T. J. Hydrogen Sulfide Adsorption on MOFs and MOF/Graphite Oxide Composites. *ChemPhysChem* **2010**, *11* (17), 3678–3684. https://doi.org/10.1002/cphc.201000689.

(21) Yang, D. A.; Cho, H. Y.; Kim, J.; Yang, S. T.; Ahn, W. S. CO2 Capture and Conversion Using Mg-MOF-74 Prepared by a Sonochemical Method. *Energy Environ. Sci.* **2012**, *5* (4), 6465–6473. https://doi.org/10.1039/c1ee02234b.

(22) Li, Z.; Liao, F.; Jiang, F.; Liu, B.; Ban, S.; Chen, G.; Sun, C.; Xiao, P.; Sun, Y. Capture of H2S and SO2 from Trace Sulfur Containing Gas Mixture by Functionalized UiO-66(Zr) Materials: A Molecular Simulation Study. *Fluid Phase Equilib.* **2016**, *427*. https://doi.org/10.1016/j.fluid.2016.07.020.

(23) Henkelis, S. E.; Huber, D. L.; Vogel, D. J.; Rimsza, J. M.; Nenoff,

T. M. Magnetic Tunability in RE-DOBDC MOFs via NOx Acid Gas Adsorption. *ACS Appl. Mater. Interfaces* **2020**, *12* (17), 19504–19510. https://doi.org/10.1021/acsami.0c01813.

(24) Vogel, D. J.; Lee, Z. R.; Hanson, C. A.; Henkelis, S. E.; Smith, C. M.; Nenoff, T. M.; Dixon, D. A.; Rimsza, J. M. Predictive Acid Gas Adsorption in Rare Earth DOBDC MOFs via Complimentary Cluster and Periodic Structure Models Predictive Acid Gas Adsorption in Rare Earth DOBDC MOFs via Complimentary Cluster and Periodic Structure Models. *J. Phys. Chem. C* **2020,** 124, 49, 26801 - 26813. https://doi.org/10.1021/acs.jpcc.0c08282.

(25) Sava Gallis, D. F.; Vogel, D. J.; Vincent, G. A.; Rimsza, J. M.; Nenoff, T. M. NOx Adsorption and Optical Detection in Rare Earth Metal–Organic Frameworks. *ACS Appl. Mater. & Interfaces* **2019**, *11* (46), 43270–43277. https://doi.org/10.1021/acsami.9b16470.

(26) Kaur, G.; Øien-ØDegaard, S.; Lazzarini, A.; Chavan, S. M.; Bordiga, S.; Lillerud, K. P.; Olsbye, U. Controlling the Synthesis of Metal-Organic Framework UiO-67 by Tuning Its Kinetic Driving Force. *Cryst. Growth Des.* **2019**, *19* (8), 4246–4251. https://doi.org/10.1021/acs.cgd.9b00916.

(27) Usman, K. A. S.; Maina, J. W.; Seyedin, S.; Conato, M. T.; Payawan, L. M.; Dumée, L. F.; Razal, J. M. Downsizing Metal–Organic Frameworks by Bottom-up and Top-down Methods. *NPG Asia Materials*. Nature Research December 1, 2020, pp 1–18. https://doi.org/10.1038/s41427-020-00240-5.

(28) Griffin, S. L.; Briuglia, M. L.; ter Horst, J. H.; Forgan, R. S. Assessing Crystallisation Kinetics of Zr Metal–Organic Frameworks through Turbidity Measurements to Inform Rapid Microwave-Assisted Synthesis. *Chem. - A Eur. J.* **2020**, *26* (30), 6910–6918. https://doi.org/10.1002/chem.202000993.

(29) Henkelis, S. E.; Vornholt, S. M.; Cordes, D. B.; Slawin, A. M. Z.; Wheatley, P. S.; Morris, R. E. A Single Crystal Study of CPO-27 and UTSA-74 for Nitric Oxide Storage and Release. *CrystEngComm* **2019**, *21* (12), 1857–1861. https://doi.org/10.1039/C9CE00098D.

(30) Forgan, R. S. Modulated Self-Assembly of Metal-Organic Frameworks. *Chemical Science*. Royal Society of Chemistry May 14, 2020, pp 4546–4562. https://doi.org/10.1039/d0sc01356k.

(31) Rezaei, F.; Rownaghi, A. A.; Monjezi, S.; Lively, R. P.; Jones, C. W. SOx/NOx Removal from Flue Gas Streams by Solid Adsorbents: A Review of Current Challenges and Future Directions. *Energy and Fuels* **2015**, *29* (9), 5467–5486. https://doi.org/10.1021/acs.energyfuels.5b01286.

(32) Li, J.; Han, X.; Zhang, X.; Sheveleva, A. M.; Cheng, Y.; Tuna, F.; McInnes, E. J. L.; McCormick McPherson, L. J.; Teat, S. J.; Daemen, L. L.; Ramirez-Cuesta, A. J.; Schröder, M.; Yang, S. Capture of Nitrogen Dioxide and Conversion to Nitric Acid in a Porous Metal–Organic Framework. *Nat. Chem.* **2019**, *11* (12). https://doi.org/10.1038/s41557-019-0356-0.

(33) Santos, S. P.; Duarte, A. P.; Bordado, J. C.; Gomes, J. F. New Process for Simultaneous Removal of CO2, SOX and NOX. *Cienc. e Tecnol. dos Mater.* **2016**, *28* (2), 106–111. https://doi.org/10.1016/j.ctmat.2016.12.002.

(34) Guan, B.; Zhan, R.; Lin, H.; Huang, Z. Review of State of the Art Technologies of Selective Catalytic Reduction of NOx from Diesel Engine Exhaust. *Applied Thermal Engineering*. Elsevier Ltd May 1, 2014, pp 395–414. https://doi.org/10.1016/j.applthermaleng.2014.02.021.

(35) Rieth, A. J.; Wright, A. M.; Dincă, M. Kinetic Stability of Metal–Organic Frameworks for Corrosive and Coordinating Gas Capture. *Nat. Rev. Mater.* **2019**, *4* (11), 708–725. https://doi.org/10.1038/s41578-019-0140-1.

(36) Jiang, H.; Niu, Y.; Wang, Q.; Chen, Y.; Zhang, M. Single-Phase SO2-Resistant to Poisoning Co/Mn-MOF-74 Catalysts for NH3-SCR. *Catal. Commun.* **2018**, *113* (February), 46–50. https://doi.org/10.1016/j.catcom.2018.05.017.

(37) Munawer, M. E. Human Health and Environmental Impacts of Coal Combustion and Post-Combustion Wastes. *J. Sustain. Min.* **2018**, *17* (2), 87–96. https://doi.org/10.1016/j.jsm.2017.12.007.

(38) Peterson, G. W.; Mahle, J. J.; Decoste, J. B.; Gordon, W. O.; Rossin, J. A. Extraordinary NO2 Removal by the Metal-Organic Framework UiO-66-NH2. *Angew. Chemie - Int. Ed.* **2016**, *55* (21), 6235–6238. https://doi.org/10.1002/anie.201601782.

(39) Tan, K.; Zuluaga, S.; Wang, H.; Canepa, P.; Soliman, K.; Cure, J.; Li, J.; Thonhauser, T.; Chabal, Y. J. Interaction of Acid Gases SO2 and NO2 with Coordinatively Unsaturated Metal Organic Frameworks: M-MOF-74 (M = Zn, Mg, Ni, Co). *Chem. Mater.* **2017**, *29* (10), 4227–4235. https://doi.org/10.1021/acs.chemmater.7b00005.

(40) Ebrahim, A. M.; Levasseur, B.; Bandosz, T. J. Interactions of NO2 with Zr-Based MOF: Effects of the Size of Organic Linkers on NO2 Adsorption at Ambient Conditions. *Langmuir* **2013**, *29* (1), 168–174. https://doi.org/10.1021/la302869m.

(41) Sava Gallis, D. F.; Rohwer, L. E. S.; Rodriguez, M. A.; Barnhart-Dailey, M. C.; Butler, K. S.; Luk, T. S.; Timlin, J. A.; Chapman, K. W. Multifunctional, Tunable Metal-Organic Framework Materials Platform for Bioimaging Applications. *ACS Appl. Mater. Interfaces* **2017**, *9* (27), 22268–22277. https://doi.org/10.1021/acsami.7b05859.

(42) Vogel, D. J.; Sava Gallis, D. F.; Nenoff, T. M.; Rimsza, J. M. Structure and Electronic Properties of Rare Earth DOBDC Metal-Organic-Frameworks. *Phys. Chem. Chem. Phys.* **2019**, *21* (41), 23085–23093. https://doi.org/10.1039/c9cp04038b.

(43) Henkelis, S. E.; Rademacher, D.; Vogel, D. J.; Valdez, N. R.; Rodriguez, M. A.; Rohwer, L. E. S.; Nenoff, T. M. Luminescent Properties of DOBDC Containing MOFs: The Role of Free Hydroxyls. *ACS Appl. Mater. Interfaces* **2020**, *12* (20), 22845–22852. https://doi.org/10.1021/acsami.0c02829.

(44) Sheldrick, G. M. SHELXT - Integrated Space-Group and Crystal-Structure Determination. *Acta Crystallogr. Sect. A Found. Crystallogr.* **2015**, *71* (1), 3–8. https://doi.org/10.1107/S2053273314026370.

(45) Sheldrick, G. M. Crystal Structure Refinement with SHELXL. *Acta Crystallogr. Sect. C Struct. Chem.* **2015**, *71* (1), 3–8. https://doi.org/10.1107/S2053229614024218.

(46) Dolomanov, O. V.; Bourhis, L. J.; Gildea, R. J.; Howard, J. A. K.; Puschmann, H. OLEX2 : A Complete Structure Solution, Refinement and Analysis Program. *J. Appl. Crystallogr.* **2009**, *42* (2), 339–341. https://doi.org/10.1107/S0021889808042726.

(47) Huq, A.; Kirkham, M.; Peterson, P. F.; Hodges, J. P.; Whitfield, P. S.; Page, K.; Hugle, T.; Iverson, E. B.; Parizzia, A.; Rennichb, G. POWGEN: Rebuild of a Third-Generation Powder Diffractometer at the Spallation Neutron Source. *J. Appl. Crystallogr.* **2019**, *52*, 1189–1201. https://doi.org/10.1107/S160057671901121X.

(48) Arnold, O.; Bilheux, J. C.; Borreguero, J. M.; Buts, A.; Campbell, S. I.; Chapon, L.; Doucet, M.; Draper, N.; Ferraz Leal, R.; Gigg, M. A.; Lynch, V. E.; Markvardsen, A.; Mikkelson, D. J.; Mikkelson, R. L.; Miller, R.; Palmen, K.; Parker, P.; Passos, G.; Perring, T. G.; Peterson, P. F.; Ren, S.; Reuter, M. A.; Savici, A. T.; Taylor, J. W.; Taylor, R. J.; Tolchenov, R.; Zhou, W.; Zikovsky, J. Mantid - Data Analysis and Visualization Package for Neutron Scattering and μ SR Experiments. *Nucl. Instruments Methods Phys. Res. Sect. A Accel. Spectrometers, Detect. Assoc. Equip.* **2014**, *764*, 156–166. https://doi.org/10.1016/j.nima.2014.07.029.

(49) Kresse; Hafner. Ab Initio Molecular-Dynamics Simulation of the Liquid-Metal-Amorphous-Semiconductor Transition in Germanium. *Phys. Rev. B. Condens. Matter* **1994**, *49* (20), 14251–14269. https://doi.org/10.1103/physrevb.49.14251.

(50) Kresse, G.; Hafner, J. Ab Initio Molecular Dynamics for Liquid Metals. *Phys. Rev. B* **1993**, *47* (1), 558–561. https://doi.org/10.1103/PhysRevB.47.558.

(51) Kresse, G.; Furthmüller, J. Efficient Iterative Schemes for Ab Initio Total-Energy Calculations Using a Plane-Wave Basis Set. *Phys. Rev. B - Condens. Matter Mater. Phys.* **1996**, *54* (16), 11169–11186. https://doi.org/10.1103/PhysRevB.54.11169.

(52) Kresse, G.; Furthmüller, J. Efficiency of Ab-Initio Total Energy Calculations for Metals and Semiconductors Using a Plane-Wave Basis Set. *Comput. Mater. Sci.* **1996**, *6* (1), 15–50. https://doi.org/10.1016/0927-0256(96)00008-0.

(53) Blöchl, P. E. Projector Augmented-Wave Method. *Phys. Rev. B* **1994**, *50* (24), 17953–17979. https://doi.org/10.1103/PhysRevB.50.17953.

(54) Joubert, D. From Ultrasoft Pseudopotentials to the Projector Augmented-Wave Method. *Phys. Rev. B - Condens. Matter Mater. Phys.* **1999**, *59* (3), 1758–1775. https://doi.org/10.1103/PhysRevB.59.1758.

(55) Perdew, J. P.; Ruzsinszky, A.; Csonka, G. I.; Vydrov, O. A.; Scuseria, G. E.; Constantin, L. A.; Zhou, X.; Burke, K. Restoring the Density-Gradient Expansion for Exchange in Solids and Surfaces. *Phys. Rev. Lett.* **2008**, *100* (13), 136406. https://doi.org/10.1103/PhysRevLett.100.136406.

(56) Vogel, D. J.; Nenoff, T. M.; Rimsza, J. M. Tuned Hydrogen Bonding in Rare-Earth Metal-Organic Frameworks for Design of Optical and Electronic Properties: An Exemplar Study of Y-2,5-Dihydroxyterephthalic Acid. *ACS Appl. Mater. Interfaces* **2020**, *12* (4), 4531–4539. https://doi.org/10.1021/acsami.9b20513.

(57) Grimme, S.; Antony, J.; Ehrlich, S.; Krieg, H. A Consistent and Accurate Ab Initio Parametrization of Density Functional Dispersion Correction (DFT-D) for the 94 Elements H-Pu. *J. Chem. Phys.* **2010**, *132* (15), 24103. https://doi.org/10.1063/1.3382344.

(58) Grimme, S.; Ehrlich, S.; Goerigk, L. Effect of the Damping Function in Dispersion Corrected Density Functional Theory. *J. Comput. Chem.* **2011**, *32* (7), 1456–1465. https://doi.org/10.1002/jcc.21759.

(59) Harvey, J. A.; Greathouse, J. A.; Sava Gallis, D. F. Defect and Linker Effects on the Binding of Organophosphorous Compounds in UiO-66 and Rare-Earth MOFs. *J. Phys. Chem. C* **2018**, *122* (47), 26889–26896. https://doi.org/10.1021/acs.jpcc.8b06198.

(60) Parkes, M. V.; Sava Gallis, D. F.; Greathouse, J. A.; Nenoff, T. M. Effect of Metal in M3(Btc)2 and M2(Dobdc) MOFs for O2/N2 Separations: A Combined Density Functional Theory and Experimental Study. *J. Phys. Chem. C* **2015**, *119* (12), 6556–6567. https://doi.org/10.1021/jp511789g.

(61) Parkes, M. V.; Greathouse, J. A.; Hart, D. B.; Sava Gallis, D. F.; Nenoff, T. M. Ab Initio Molecular Dynamics Determination of Competitive O2 vs. N2 Adsorption at Open Metal Sites of M2(Dobdc). *Phys. Chem. Chem. Phys.* **2016**, *18* (16), 11528–11538. https://doi.org/10.1039/c6cp00768f.

(62) Li, Y.; Wang, X.; Xu, D.; Chung, J. D.; Kaviany, M.; Huang, B. H2O Adsorption/Desorption in MOF-74: Ab Initio Molecular Dynamics and Experiments. *J. Phys. Chem. C* **2015**, *119* (23), 13021–13031. https://doi.org/10.1021/acs.jpcc.5b02069.

(63) Zeolite Molecular Sieves: Structure, Chemistry, and Use D. W. Breck (Union Carbide Corporation, Tarrytown, New York) John Wiley and Sons, New York, London, Sydney, and Toronto. 1974. 771 Pp. $11.95. *J. Chromatogr. Sci.* **1975**, *13* (4), 18A-18A. https://doi.org/10.1093/chromsci/13.4.18a-c.

(64) Rubel, A. M.; Stencel, J. M. Effect of Pressure on NOx Adsorption by Activated Carbons. *Energy and Fuels* **1996**, *10* (3), 704–708. https://doi.org/10.1021/EF9501861.

(65) Dangelo, P.; Zitolo, A.; Migliorati, V.; Chillemi, G.; Duvail, M.; Vitorge, P.; Abadie, S.; Spezia, R. Revised Ionic Radii of Lanthanoid(III) Ions in Aqueous Solution. *Inorg. Chem.* **2011**, *50* (10), 4572–4579. https://doi.org/10.1021/ic200260r.

(66) Cordero, B.; Gómez, V.; Platero-Prats, A. E.; Revés, M.; Echeverría, J.; Cremades, E.; Barragán, F.; Alvarez, S. Covalent Radii Revisited. *J. Chem. Soc. Dalt. Trans.* **2008**, No. 21, 2832–2838. https://doi.org/10.1039/b801115j.

(67) Øien-ØDegaard, S.; Shearer, G. C.; Wragg, D. S.; Lillerud, K. P. Pitfalls in Metal-Organic Framework Crystallography: Towards More Accurate Crystal Structures. *Chemical Society Reviews*. Royal Society of Chemistry August 21, 2017, pp 4867–4876. https://doi.org/10.1039/c6cs00533k.

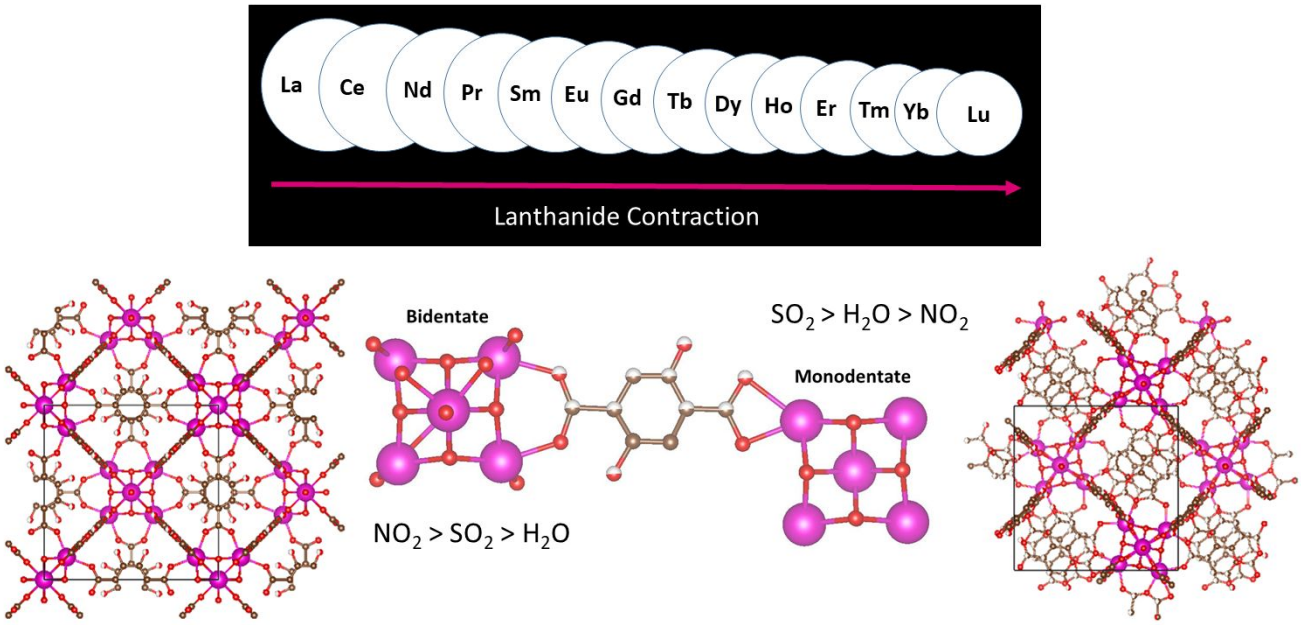
La
Ce
Nd
Pr
Sm
Eu
Gd
Tb
Dy
Ho
Er
Tm
Yb
Lu
Lanthanide Contraction
Bidentate
Monodentate
$SO_2 > H_2O > NO_2$
$NO_2 > SO_2 > H_2O$